Chemical Science

ROYAL SOCIETY OF CHEMISTRY

EDGE ARTICLE

View Article Online
View Journal | View Issue

Cite this: *Chem. Sci.*, 2020, **11**, 5950

All publication charges for this article have been paid for by the Royal Society of Chemistry

Received 17th December 2019
Accepted 16th May 2020

DOI: 10.1039/c9sc06386b

rsc.li/chemical-science

Deconvolution of electroosmotic flow in hysteresis ion transport through single asymmetric nanopipettes†

Warren Brown, Yan Li, Ruoyu Yang, Dengchao Wang, Maksim Kvetny, Hui Zheng and Gangli Wang *

Unveiling the contributions of electroosmotic flow (EOF) in the electrokinetic transport through structurally-defined nanoscale pores and channels is challenging but fundamentally significant because of the broad relevance of charge transport in energy conversion, desalination and analyte mixing, micro and nano-fluidics, single entity analysis, capillary electrophoresis *etc.* This report establishes a universal method to diagnose and deconvolute EOF in the nanoscale transport processes through current–potential measurements and analysis without simulation. By solving Poisson, Nernst–Planck (PNP) with and without Navier–Stokes (NS) equations, the impacts of EOF on the time-dependent ion transport through asymmetric nanopores are unequivocally revealed. A sigmoidal shape in the *I*–*V* curves indicate the EOF impacts which further deviate from the well-known non-linear rectified transport features. Two conductance signatures, an absolute change in conductance and a 'normalized' one relative to ion migration, are proposed as EOF impact (factor). The EOF impacts can be directly elucidated from current–potential experimental results from the two analytical parameters without simulation. The EOF impact is found more significant in intermediate ionic strength, and potential and pore size dependent. The less-intuitive ionic strength and size dependence is explained by the combined effects of electrostatic screening and non-homogeneous charge distribution/transport at nanoscale interface. The time-dependent conductivity and optical imaging experiments using single nanopipettes validate the proposed method which is applicable to other channel type nanodevices and membranes. The generalizable approach eliminates the need of simulation/fitting of specific experiments and offers previously inaccessible insights into the nanoscale EOF impacts under various experimental conditions for the improvement of separation, energy conversions, high spatial and temporal control in single entity sensing/manipulation, and other related applications.

The transport of charged species and solvent flow in nano-apertures can be generated through an applied potential-electrokinetic transport including electroosmotic flow (EOF), pressure differential, or concentration gradient *etc.* The transport processes, ions or neutral species without or with solvent flow, play important roles in many applications such as detection analysis[1–7] in particular the manipulation and controls toward single entities (molecules/nanoparticles/cells),[8–10] net pumping of analyte,[11–13] separation in capillary electrophoresis (micron-sized channels) and microfluidics,[14,15] and energy conversion.[16,17] The redistribution of ions during the transport process changes electrical double layer (EDL) structure. Because EOF arises from the interplay of EDL with externally applied electrical field, studies on EOF and nanoscale EDL are at the transition regime bridging the two fields of nano-electroanalytical chemistry and electrophoresis. Studies on EOF contributations in nanotransport have been limited by theory/simulation under constant potentials or steady-state. EOF in time-dependent electrokinetic ion transport in nanopores or nanochannels remain one of the essential questions to be addressed despite the extensive studies recently.

Non-bulk transport phenomena emerge when the contributions from the EDL regions on charged asymmmetric nanopore/channel walls cannot be ignored, for example when at least one dimention of the nanodevices is 'close' to the Debye length of the EDL. The Debye length is a classic descriptor of the EDL that is a function of solution ionic strength, solvent relative permittivity and temperature *etc.* (expression for calculation included in ESI†).[18]

Department of Chemistry, Georgia State University, Atlanta, GA 30302, USA. E-mail: glwang@gsu.edu

† Electronic supplementary information (ESI) available: Details of the simulation; details of the analysis; and experimental examples from different nanopipettes and intermediate concentrations from the examples in the text (PDF). See DOI: 10.1039/c9sc06386b

The comparison to Debye length has two often misleading aspects of (1) an inaccurate underlying assumption of uniform transport through the channel cross section, and (2) the overall surface effect is limited strictly to the Debye length which in fact describes the percentage drop of surface electrical field. In other words, the channel can be significantly larger than the Debye length yet surface affected transport behaviors remain distinct or cannot be ignored. Ion migration (or electrophoresis) through channel-type nanodevices is influenced by the combined applied (across the nanopore/channel) and surface (vector component in the direction of transport) electrical fields. Asymmetry in nanochannel structures, such as the prototype conical nanopores studied herein,[18,19] together with surface charges and modifications,[14,20–22] provide materials/device platforms for selective transport. The well-known ion current rectification (ICR) results from the enhancement and depletion of ions as charge carriers which causes different ion flux under opposite polarities of the same applied potential magnitudes. When the applied potential varies over time, for example sweeping cyclically like in cyclic voltammetry, transient or dynamic ion redistribution under varying stimulus induces interesting phenomena such as pinched hysteresis loops and a non-zero cross point in current–potential curves.[23–26]

EOF in the transport through nanoapertures under variable stimulus has not been explored to the best of our knowledge. The role of EOF in the nanotransport is mostly studied under a constant potential or steady-state by simulation because experiments mostly measure the overall transport current/flux. Unfortunately, the EOF contributions in simulation literature ranged from negligible/detectable,[27–29] somewhat significant[30] and more recently to significant under various salt, ionic strength, geometric and surface charge density conditions.[31–34] Electroosmotic flow rectification (EFR), *i.e.* asymmetric flow, is reported to arise from the concentration polarization process, resulting in different current values or flow rates at potentials of the same magnitude but opposite polarities respectively.[35] EFR has been demonstrated in nanopores with asymmetric solvent or solution combinations[36,37] and in asymmetric pores[11,38] or membranes[12,13,39,40] in symmetric electrolyte conditions. Related phenomena such as negative differential resistance have been generated from the same underlying EOF mechanism.[41,42] The impacts by pressure driven flow on the concentration polarization process in conical nanopores have also been reported.[43]

This report presents a solution to analyze EOF directly from experimental current–potential measurements, by firstly establishing the methodology *via* simulation, and then validation with electroanalytical and imaging experiments. As illustrated in Scheme 1, using a single conical nanopipette as prototype, analytical signatures of EOF can be obtained directly from current–potential curvatures. While non-linearity in *I–V* curve is well-known indication of surface affected transport, a sigmodal shape, or derivatives in terms of conductance/conductivity, reveals strong EOF effect.

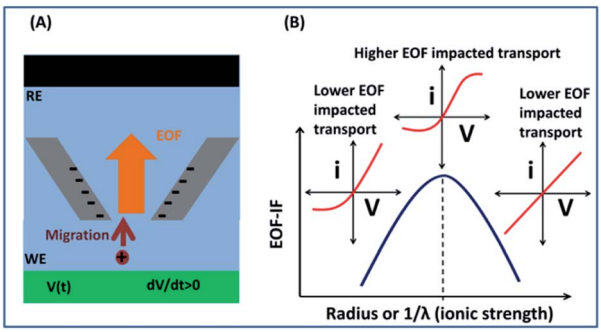

Scheme 1 (A) Experimental and simulation setup of transport through a single nanopipette with negative surface charges in solution. The directions are sketched corresponding to high conductivity state. A potential is applied on the working electrode (WE/green, bottom) with respect to the reference electrode (RE/black, top). When the bias is positive, the high conductivity state is established with facilitated transport of cations as the majority charge carrier. The light red arrow indicates the direction of migration; and orange arrow indicates the direction of EOF. (B) Impact of EOF on the conductivity measurements at different limiting dimension of the device, either the radius or the ionic strength effect described by the Debye length (λ). The three red *i–V* sketches represent diagnostic features of non-linear shape for ICR, sigmodal for EOF presence, and more linear ohmic behaviors.

Experimental methods

Fabrication of nanopipettes was carried out using a laser puller (P-2000 Sutter) and quartz capillaries (O.D.: 1.0 mm, I.D.: 0.7 mm). To fabricate relatively small nanopipettes the pull parameters were: heat: 700, filament: 4, velocity: 60, del: 150, pull: 120 or 155. For larger nanopipettes a two-line pull was used (1) heat: 750, filament: 4, velocity: 55, del: 180, pull: 80. (2) heat: 700, filament: 4, velocity: 60, del: 150, pull: 150 or 120. The nanopipette was loaded in the sequence of: acetonitrile, water and KCl electrolyte *via* centrifugation. The sizes of individual nanopipettes were calculated based on the conductance following standard procedures previously reported and detailed in ESI.†

A Gamry Reference 600 (Gamry Co.) was used for measuring the conductivity. The analyzed data were collected with the scan rate of 300 mV s^{-1} which was neither optimized nor limiting for EOF effects. The electrical potential was applied through two silver/silver chloride wires in inside and outside solutions. The bias polarity is defined with respect to the electrode positioned on the base side (inside capillary). The first scan of conductivity measurements was discarded, and later scans overlap confirming reproducibility.

Optical images were recorded with an Olympus BX51 microscope using a 40 X Olympus LumPlanFLN water immersion objective. Rhodamine B (Sigma-Aldrich) at 10 μM was loaded inside nanopipettes which were mounted on microscope slide, whose fluorescence was excited with X-Cite 120 Q and detected with Lumenera Infinity 3s monochrome camera. A Dagan ChemClamp amplifier with a Dagon 100 M head stage preamp was used to apply potential during imaging. At each potential images were taken every 200 ms at an exposure time of 100 ms. The images were processed with Image J version 1.4 using Micromanager 1.4.22 and Plot Profile.

Finite element modelling

COMSOL Multiphysics (version 4.3, with 'transport of diluted species', 'electrostatics' and 'laminar flow' modules) were used

for finite element modeling of the transport through quartz nanopipettes. The simulation method follows our previous reports that have successfully modelled the experimental conical nanopore electrokinetic responses under various salinity and input stimulus dynamics (potential scan rate, ν).[23,24,26,44] In other words, the applied potential is defined as a variable ($V = V_0 + \nu_t$). The Poisson, Nernst–Planck (PNP) and Navier–Stokers (NS) equations are coupled to calculate the electrical fields, ion flux and electroosmotic flow (EOF). The conical nanopore structures, surface charge definition, additional simulation details, and further explanations of the governing equations are provided in the ESI.† It is worth mentioning that the adjustment of SCD values or the conical nanostructures will not affect the observed trends/analysis; it only changes the absolute current/conductance values.

The Nernst–Planck shown in eqn (1) is used to simulate the flux of the ions:

$$J_i = -D_i\nabla c_i - \frac{z_i F}{RT} D_i\, c_i \nabla\phi + c_i \boldsymbol{u} \quad (1)$$

J_i is the flux of an individual ion; D_i is the diffusion coefficient of the ion; c_i is the concentration of the ion; z_i is the charge of the ion; F is Faraday constant; R is the gas constant; T is the temperature; ϕ is the electric potential and $\boldsymbol{u}$ is the fluid velocity. The first term in eqn (1) represents flux from diffusion, the second from migration and the third convective flux from fluid flow.

The Poisson equation (eqn (2)) calculates the electric fields and ion distribution:

$$\nabla^2(\varepsilon_0\varepsilon_r\phi) = -F\sum z_i c_i \quad (2)$$

ε_0 and ε_r are the relative permittivity of free space and the solvent respectively.[26,45]

The Navier–Stokes equation (NS), shown as eqn (3), calculates the fluid flow and therefore the flux from convection in the third term in eqn (1). Under continuity with the incompressible solvent, the Navier–Stokes (NS) equation equals zero:

$$\frac{1}{\rho}\left(-\nabla p + \eta\nabla^2\boldsymbol{u} - \left(F\sum z_i c_i\right)\nabla\phi\right) = 0 \quad (3)$$

ρ, η is the density and viscosity of the solvent respectively, and p is the applied pressure which is zero herein. The second term in eqn (3) is the dragging due to solvent viscosity and the third is the driving force component which in this case is an electric force defining the electroosmotic flow.

Results and discussion

Simulated current–potential measurements with and without EOF consideration

Characteristics of EOF impact on the ion transport conductance. Simulated conductivity measurements without EOF (PNP) and with EOF (PNP–NS) are compared in Fig. 1 panel (A). In the transient regime, in contrast to for example, those under individual constant potentials, frequency dependent additional features are observed such as a non-zero cross point (V_{cp}) demarcated by the dashed line. The cross point represents

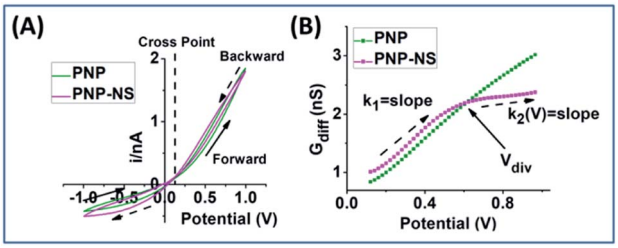

Fig. 1 Simulated conductivity and differential conductance (G_{diff}) analysis. (A) Conductivity measurement by PNP (olive) and PNP–NS (magenta) of a 12 nm radius nanopore in 1 mM KCl. Dashed line indicate the position of the cross point (CP); arrows indicate the direction of the applied potential with solid arrows defining forward and dashed arrows backward scans. (B) Differential conductance (G_{diff}) analysis for forward scan in the PNP and PNP–NS model. k_1 and k_2 are the slopes before and after the deviation of G_{diff} (V_{div}) from the PNP and PNP–NS models.

the average surface electrical field effects in the direction of ion transport, *i.e.* along the axial direction inside the nanopore, and indicates the transition between high conductivity states (HC, positive bias defined as outside *vs.* inside) and low conductivity states (LC). The hysteresis loops between the non-overlapping forward and backward current curves at HC and LC arise due to lagging in the concentration polarization with respect to the changes in the potential stimulus and reveal the total charges enriched at HC or expelled at LC within the cycles of external potential stimulus.[44] When EOF is considered by coupling NS equation, the rectification of ionic current is attenuated, *i.e.* the current at HC is generally lower while at LC the current is higher compared to the PNP model results. The cross point potential is not affected by the inclusion of EOF because the surface electric field arises from the deprotonation of silanol groups and gives rise to EOF.

The potential-dependent differential conductance (G_{diff}) in HC is plotted in Fig. 1 panel (B) where $G_{diff} = \mathrm{d}i/\mathrm{d}V$, *i.e.* the slope of an i–V branch. The differential conductance is used instead of the conductance (i/V) because it more sensitively reveals EOF as signatures as demonstrated in Fig. S1.† The G_{diff} has a similar slope from PNP and PNP–NS models at lower potentials, defined as k_1, up to a divergent point V_{div} after which EOF impact becomes more significant. The forward current in HC is used to establish the signature of EOF impact because it displays the most straightforward prominent features. Fig. S2† provides the analysis of other branches. Out of the four current branches separated by the cross point, the scans toward the cross point are affected by the end/switching potential which varies and is often arbitrarily selected in measurements. The EOF effect at LC is generally not as significant as HC especially in smaller pores or lower ionic strength because of the depletion of mobile charge carriers elaborated in later sections.

The common slope region basically reflects the conductance from ion migration governed by the overall electrical field (applied and surface) in the nanopore. Deviations from the PNP results toward higher potentials therefore correspond to the

EOF impacts, indicated by the clearly different slopes of k_2. Because experimentally, there will only be one overall conductivity responses (not two curves as shown from simulation), it is convenient and significant to employ the common response in low potential range as reference (*i.e.* k_1) for the evaluation of the EOF both qualitatively and quantitatively.

Two parameters are proposed that describe (1) the absolute EOF impact (EOF-I) and (2) a dimensionless EOF impact factor (EOF-IF), both relative to the electrokinetic transport (PNP) measured in low potential range (k_2 *vs.* k_1). The EOF-I, with the unit of nS, measures the suppression of differential conductance by EOF at different potentials in a given bulk electrolyte concentration.

$$\text{EOF-I} = (k_1 - k_2) \times V = G_{\text{diff}}^{\text{PNP}} - G_{\text{diff}}^{\text{PNP–NS}} \quad (4)$$

The EOF-IF can be expressed in %. A zero EOF-IF, *i.e.* $k_2 = k_1$, means no EOF (PNP results or pure migration). Increase in EOF will decrease k_2 and give a larger EOF-IF value. At $k_2 = 0$ or EOF-IF at 100%, EOF matches the migration in absolute values (but negatively, or reduction) to the measured differential conductance. Even stronger EOF could make the k_2 negative and thus an EOF-IF greater than 100%, which corresponds to the EOF outweighing the remaining migration in absolute values.

$$\text{EOF-IF}\ (\%) = \frac{k_1 - k_2}{k_1} \quad (5)$$

Two representative sizes are chosen in simulation, each with experimental *i–V* data in a series of ionic strength for validation. The features are representative as confirmed by other nanopipette in the comparable size ranges in experiments.

Ionic strength effects. Simulation results of a 12 nm radius nanopore in different KCl concentrations are shown in Fig. 2. As concentration increases from 1 mM to 100 mM, the differences in current at HC between the PNP and PNP–NS models increase (panels A–C). Clearly the current decrease at HC is more significant over the current increase at LC when EOF is considered. In the corresponding differential conductance G_{diff} plots at HC (panels D–F), the common slope k_1 and the deviations k_2 at relatively low and high bias range, separated by a diverging point V_{div}, is apparent between the two models. At LC, the divergence of G_{diff} of PNP–NS from PNP toward higher bias is only obvious at higher ionic strength, with the curve shape mirroring HC. The less significant EOF at LC is attributed to less mobile charge carriers to drive EOF, the same principle to explain the high resistance due to the concentration depletion in ICR or ion concentration polarization.[36,46]

EOF-I and EOF-IF from PNP–NS data are plotted in Fig. 3. k_1 is calculated from the linear fitting of G_{diff} slope within the common region up to the divergent potential V_{div} between PNP and PNP–NS models. The fittings are provided in Fig. S3.† k_1 represents the conductance region where EOF effects are insignificant and is therefore suitable as reference for normalization (within the same nanodevice under different measurement conditions, as device heterogeneity can be inevitable in experiments). k_1 increases with electrolyte concentration or charge carriers, but non-linearly as shown in Fig. S4† because of the surface effects.

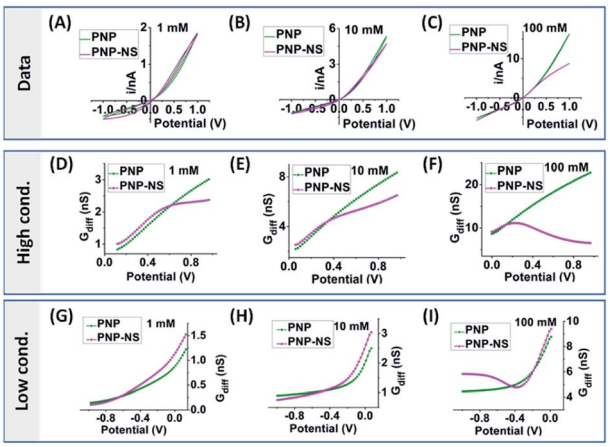

Fig. 2 Simulated conductivity measurements from PNP (olive) and PNP–NS (magenta) with a 12 nm radius nanopore in (A) 1 mM; (B) 10 mM; (C) 100 mM. Differential conductance analysis at HC in (D) 1 mM (E) 10 mM (F) 100 Mm; and at LC (G) 1 mM (H) 10 mM (I) 100 mM.

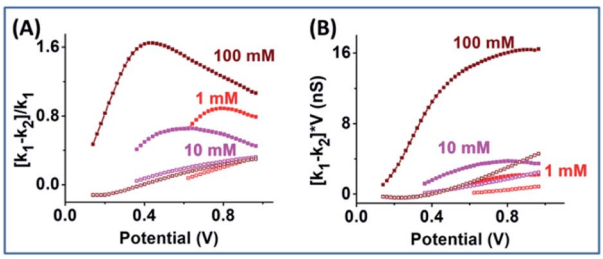

Fig. 3 Simulated response from PNP–NS (top curves) and PNP (bottom curves) with a 12 nm radius nanopore for (A) EOF-IF and (B) EOF-I at 1 mM (red), 10 mM (magenta) and 100 mM (wine). Note the starting potential V_{div} varies with ionic strength.

k_2 is calculated from the second derivative $k_2\,(\text{V}) = \text{d}G_{\text{diff}}/\text{d}V$ because the G_{diff} region after the divergent V_{div} is non-linear. Fig. S5† provides second derivative analysis of PNP–NS results, together with PNP results for comparison. It is found that the peaks in the second derivative profiles in both models are similar in value to fitted k_1 and can be used to directly obtain k_1. This feature is favorable for the analysis of experimental results in which noise and available data points within the linear range can vary. In this report, the fitted k_1 is used in the simulation analysis, while the peak value in the second derivative is used in the analysis of the experimental results. The approach is validated in Fig. S6† by the linear correlation (slope ~1) between the two k_1s from fitting and the peak.

EOF-IF passes the first evaluation at the boundary condition when $k_1 = k_2$, EOF-IF equals zero, or there is no EOF. A larger or more positive EOF-IF suggests stronger EOF which reduces the measured conductance. At all concentrations the two EOF parameters show a similar peak shaped dependence on the potential, *i.e.* G_{diff} suppression increases and then either decreases or plateau toward high potential tested. The peak

potential shifts lower toward cross point as ionic strength increases. In 100 mM, in Fig. 3 panel A, the EOF-IF has a maximal value of ~1.6 which also corresponds to the sigmoidal conductivity measurement in Fig. 2 panel C. The sigmoidal response is therefore characteristic of the EOF impact on the transport: better defined or stronger sigmoidal shape indicates stronger EOF.

The potential and concentration effects can be explained by the interplay and balance of concentration polarization affected by rectified ion migration and EOF. In the negatively charged nanopores, EOF depends on the available cation flux in the double layer within the transport-limiting nanopore region. However, if the ionic strength is too high, *i.e.* hundreds of milli-M for tens-nm nanopores, electrostatic screening will reduce EOF effect. Loss or diminishment of ion current rectification can be a qualitative indication of the ionic strength being too high. Because ion distribution within nanopore is potential dependent,[35,47] the relative dimension/volume of EDL *versus* nanopore varies. At HC, concentration polarization further enhances ion concentration in the nanopore at higher potentials, which also incurs stronger electrostatic screening. Correspondingly, the EOF increases initially and then decreases under increasing applied scanning potential. A lower bulk concentration requires a higher applied potential to reach the point of maximal EOF effects on the ion transport. Correspondingly, the peak shifts to lower potentials at higher bulk electrolyte concentration. Similar trends can be seen by analyzing the scans to more negative potentials at LC in Fig. 2. Following the same rationale, EOF effect will decrease, *i.e.* both EOF-IF and EOF-I peaks decrease and shift to higher potentials at higher scan rates (Fig. S7†) similar to ICR because less concentration polarization occurs within shorter time under stimulus.

It is important to understand that the potential range affects the validity of EOF-IF and EOF-I. Both EOF-IF and EOF-I were calculated with respect to the transport at lower potential region dominated by migration. For example, the EOF-I can be qualitatively perceived as $G_{PNP} - G_{PNP-NS}$ where the two terms originate from lower potential range and the potentials of interest respectively. The corresponding curves calculated from PNP results (more positive than V_{div}) demonstrate the theoretical limit of this analysis. The non-zero curves from PNP model are caused by the approximation of linear extrapolation of k_1 after the divergent point, where non-linear rectified electrokinetic transport or the non-linear concentration polarization is known to occur.

Size effects. Fig. 4 & 5 present the results from a 60 nm nanopore. The *i–V* conductivity, especially in HC, shows a significantly larger current difference between the PNP and PNP–NS results. In general, EOF has a more significant impact on the conductivity features in the larger nanopore than the smaller nanopore: both the current decrease at HC and the current increase at LC at higher ionic strength are more significant after the N–S equation is coupled to the PNP in the model. A sigmodal shape in *i–V* curve (5 & 10 mM) is a distinct feature to qualitatively diagnose EOF presence. The sigmoidal feature occurs at lower concentration when the pore is larger.

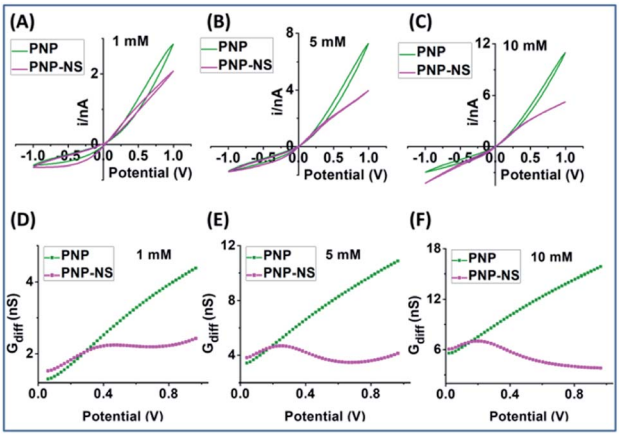

Fig. 4 Simulated conductivity measurements from PNP (olive) and PNP–NS (magenta) with a 60 nm radius nanopore in (A) 1 mM; (B) 5 mM; (C) 10 mM. Differential conductance analysis in (D) 1 mM (E) 5 mM (F) 10 mM.

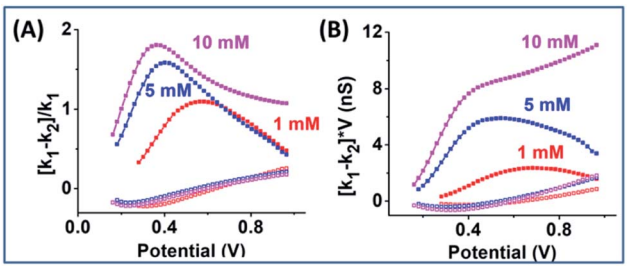

Fig. 5 Simulated response from PNP–NS (top curves) and PNP (bottom curves) with a 60 nm radius nanopore for (A) EOF-IF and (B) EOF-I at 1 mM (red), 5 mM (blue) and 10 mM (magenta).

The differential conductance G_{diff} in panels (D–F) displays a common slope region for k_1 determination but decrease more sharply after the divergent potential V_{div} which shifts toward the cross point from 1–10 mM. The narrower linear low potential range in panel F further attests the needs to employ the peak values in the dG_{diff}/dV to determine k_1 rather than *via* fitting explained in Fig. S5 and S6.† A lower V_{div} and larger decrease in G_{diff} in the PNP–NS indicate more significant EOF effect in the larger nanopore. The corresponding current branches at LC from cross point toward negative are shown in Fig. S8,† which displays stronger curve divergence at higher ionic strength similar to the trend observed in smaller nanopores.

The EOF-IF plotted in Fig. 5 panel (A) is larger than those from the smaller nanopore at all potentials and concentrations. A maximum of EOF-IF is better resolved with the larger nanopore because G_{diff} decrease more sharply toward higher potentials indicating stronger EOF impacts. While the EOF-IF max is about 80% (of the migration as reference) in the 12 nm nanopore between 1 mM and 10 mM, the IF max in the 60 nm nanopore appears to reach a threshold approaching 200%, *i.e.* the EOF is twice the differential conductance by migration (but negative or reducing). An even higher ionic strength (bulk concentration and/or potentials) will greatly suppress surface

field effect, and thus make ICR and hysteresis harder to resolve. The IF max positions are lower for the larger radius nanopore for all concentrations compared to the smaller nanopores as plotted in Fig. S9.† This corresponds to a higher flow rate resulting from the larger radius requiring less positive potential.[36] It is worth mentioning that the ion flux is well-known to be non-uniform within nanopore cross-section and is highest along the interface, which explains the prominent surface effects. Similarly, the larger EOF-I value and larger potential range with a relatively constant EOF-I, *i.e.* plateau, in panel B at 10 mM originates from the larger EOF in the 60 nm nanopore and the competing enhancement/screening effects.

Experimental results for the validation of EOF signatures

The key EOF diagnostic features from simulation include: qualitatively (1) the sigmodal *i–V* curve shape and (2) the peak-shaped or non-linearly decreased differential conductance toward higher potentials; and quantitatively (3) the potential dependent EOF-I and EOF-IF whose curve shape and peak positions are dependent on ionic strength. Representative experimental results with clear EOF effects are presented for qualitative validation first. In Fig. 6, the sigmodal *i–V* shape appears at much lower potential, around 0.5 V in (D) from a larger nanopore than a smaller one in (A). While the signature of G_{diff} curve shape at HC is obvious for both cases, the deviations at LC is only distinguishable when EOF is sufficiently strong (panel F). The need to project trajectories (arrows in panels B, E & F) attests to the experimental challenges to resolve EOF and the significance of normalization/reference within the same data, *i.e.* k_2 *versus* the k_1 at lower potentials, in stark contrast to simulation where PNP and PNP–NS results can be calculated separately. Further, the plots of EOF-I and EOF-IF from two nanopores (~200 nm) with strong EOF are shown in Fig. S10,† both displaying obvious peak shaped curves in excellent agreement with simulation.

To provide guidance for the analysis of experiments where EOF effects are less obvious, more systematic experimental results from relatively medium and small sized nanopipettes in a range of electrolyte concentrations are analyzed. Representative results from low, medium and high concentrations are plotted in Fig. 7 & 8, with additional concentrations included in Fig. S11 and S12.† The comprehensive view is believed useful for the general adoption of this analytical method to other nanostructures/surfaces as long as adequate characterizations in geometry and surface charge density are accessible.[48] Similar to the simulated PNP–NS responses from the larger nanopore in Fig. 4, the measured *i–V* features in Fig. 7A transit from the expected rectified response in low electrolyte concentration, to a sigmoidal shape in 100 mM, and to more linear ohmic

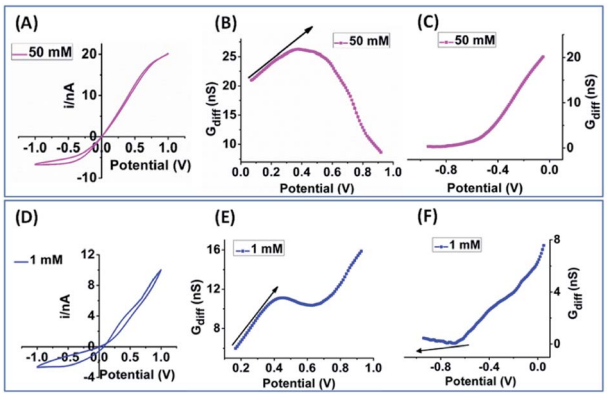

Fig. 6 Experimental results from a 60 nm nanopore in 50 mM KCl (A–C) and a 200 nm nanopore in 1 mM KCl solution (D–F). The arrows in (B, E and F) suggest trajectories without EOF.

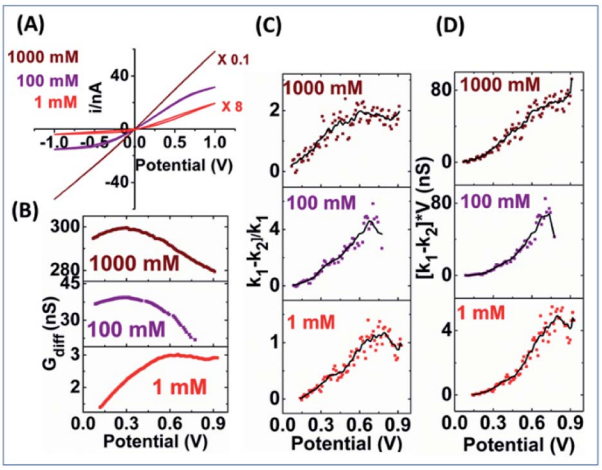

Fig. 7 Experimental *I–V* data (A) and corresponding analysis of G_{diff} (B), EOF IF (C) and EOF-I (D) from a large nanopipette (with *ca.* 60 nm radius) in different KCl concentrations. The black curves are generated by smoothing the scattered data points (EOF-IF and EOF-I) using a 20 point window. Some curves are multiplied by the listed arbitrary factors to fit in the same scale for direct visual comparison.

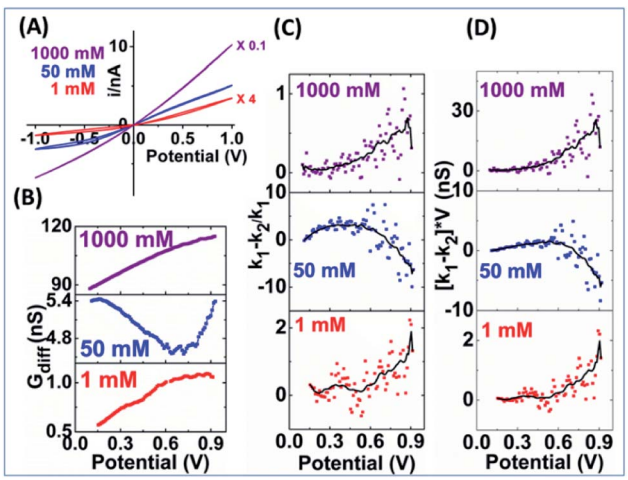

Fig. 8 Experimental *I–V* data (A) and corresponding analysis of G_{diff} (B), EOF IF (C) and EOF-I (D) from a small nanopipette (with *ca.* 10 nm radius) in different KCl concentrations. The black curves are generated by smoothing the scattered data points (EOF-IF and EOF-I) using a 20 point window. Some curves are multiplied by the listed arbitrary factors to fit in the same scale for direct visual comparison.

behavior in 1 M due to more effective screening of the surface charge. As predicted in simulation, more obvious sigmoidal shape indicates greater EOF impact on the transport conductance that occurs at intermediate ionic strength. In G_{diff} plots, the decrease toward higher potentials that clearly deviates from the increase (linear trend) in lower potential range, the shift in peak position to less positive at higher ionic strength and better-defined curve shape are also consistent with simulation.

The EOF-IF and EOF-I curves describe EOF impacts at different potentials. Since noise is inevitable in experiments which can be 'amplified' in derivatives (2^{nd} for k_2), it is important to focus on whether the overall trend is consistent with simulation. Though less prominent than those in Fig. S10,† the peaked curve shapes are reminiscent of the PNP–NS simulation results. Among all concentrations (shown in Fig. S11†), the EOF-IF maximizes at around 100 mM, with the peak/plateau at less positive potential at around 0.5–0.7 V. Although the EOF-I in panel D is larger in 1000 mM, one should keep in mind that conductance is higher with more charge carrier, *i.e.* higher ion concentrations. As indicated by the EOF-IF, EOF has a more significant impact on the transport over migration/electrophoresis in 100 mM compared to 1000 mM. It is also significant to notice that even in conditions where apparent ohmic behavior is approached, EOF can still have a detectable influence on transport.

The greater oscillatory 'noisy' responses at higher potentials, less at low ion concentrations, might not be solely due to experimental noise, as random noise would be consistent within one dataset or series of measurements. Outlier rejection, boxcar average and smoothing (described in ESI, Fig. S13†) do not eliminate those 'noise' even after significant distortion of expeirmental data is observed. We speculate complications from stochastic or random processes, such as nucleation, nanoprecipitation, bubble formation, as well as the competing mechanisms of nanopore concentration polarization and electrostatics screening *etc.*[49–51] Further considerations on those aspects, currently underway, are beyond the scope of this report and do not affect the key conclusions.

The measured *i–V* results from a smaller nanopore in Fig. 8 panel A show current rectification up to 1 M, but a sigmoidal shape can only be arguably discerned visually at 50 mM. The EOF can be better resolved in the G_{diff} plots. Unlike the largely linear increase in G_{diff} toward higher potentials at other concentrations, the 50 mM curve in panel B decreases to a minima at about 0.8 V indicating more significant EOF impact. Accordingly, peak shaped curves are only resolved from the 50 mM data for the two EOF charactors in panels C & D which are generally lower than those for the larger nanopipette. These results are broadly consistent with the modelling results which predict that larger nanoaperatures have larger EOF. The lower EOF in the smaller nanopipettes also means narrower conditions such as ionic strength range to resolve the EOF. Another observation is that at 50 mM the EOF-IF reaches maximum then decreases to negative values toward higher potentials. The negative EOF-IF can also be seen in simulation results, albeit less distinct within the potential range limited to ±1 V (to be more relevant to experiments where bubble formation due to water splitting should be avoided). A possible explanation that requires further study is the significant concentration enhancement at higher potentials which attenuates the EOF. Additional examples from other nanopipettes are provided in Fig. S14 and S15† to offer a range of behaviors that will be observed in different experimental systems. Overall, the same qualitative trends are observed and consistent with simulation, while the quantitative factors and features vary due to variations in geometry and surface charge density of the fabricated nanopipettes.

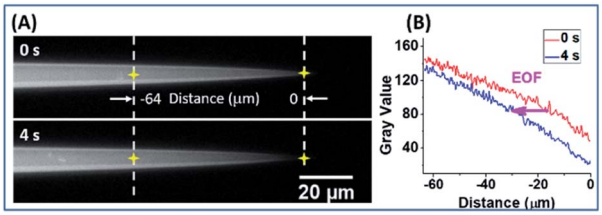

Fig. 9 Fluorescence imaging of EOF in a *ca.* 60 nm radius nanopipette in 50 mM KCl solution. The interior solution also contains 10 μM rhodamine B. (A) Representative frames (taken at time zero and 4s after +1 V was applied). (B) Comparison of the 0s and 4s intensity profiles along the centerline between the yellow crosses. The distance was demarcated by the dashed lines. The background, contrast and size of all time-lapse images are set consistent for direct comparison of grey scale intensity.

Imaging of EOF in nanopipettes

Next EOF is directly observed by the changes in fluorescence intensity. Rhodamine B is neutral under the measurement condition (unbuffered, slightly acidic between 6–7 due to varied CO_2 dissolution).[52] Therefore, the movement of the dye results solely from the EOF without the complication of electrophoresis effect. Rhodamine B was added only to the solution inside the nanopipettes but not outside, with the other conditions comparable to the conductivity measurements. The changes in emission intensity over time under +1 V are presented in Fig. 9. The intensity near the tip area decreases within seconds (Panel A, additional images in S16†), demonstrating the direction of EOF is toward inside capillary, because rhodamine B was not added in the exterior solution. Corresponding intensity analysis in panel B further reveal the left-shift of the fluorescence profiles or the EOF effect semi-quantitatively. Time lapse images under 0 V and −1 V are provided in ESI Fig. S17† as controls. Under negative potential, EOF or cation flux is toward the outside of the nanopipette. The fluorescence profiles shift right, or the intensity increases near the tip. It is worth mentioning that the dyes, either *via* diffusion or by EOF into the outside bulk solution, will be mostly out of focus and not affect the image analysis.

Conclusion

The electroosmotic flow contribution to the overall electrokinetic transport through single nanopipettes is deconvoluted by

simulation and confirmed by experiments. By comparing the current–potential curves with and without flow consideration in continuum-based simulation, a sigmodal shape is identified as qualitative diagnostic feature of EOF presence. Two quantitative parameters for the EOF impact proposed: an absolute EOF impact describing the suppression in conductance by EOF; and a relative EOF impact factor in reference to the migration/electrophoresis from the same device/solution conditions. Importantly, both parameters can be elucidated from a single experimental *i–V* curve. The analytical characteristics of EOF contribution are validated by surveying nanopipettes of different size ranges and under different electrolyte concentrations. In general, EOF is stronger in intermediate ionic strength and for radius much larger than the Debye length. For a given nanodevice in a given bulk electrolyte solution, EOF impacts increases from zero volts or cross-point potential, reaches a maximum or plateau at intermediate potential ranges, and then decreases at higher potential range depending on the measurement condition. Successful imaging of the nano-confined EOF with a neutral fluorophore not just validates the proposed method; it also provides EOF as another mechanism for single entity handling of charged as well as neutral species, and possibly improved controls. It is important to emphasize that nanopore results are well known to be susceptible to heterogeneity in device nanogeometry and surface charge variations, which is inaccessible for quantitative fitting. The self-calibration proposed herein, EOF characteristics in reference to the migration electrokinetic transport from the exact same measurement, is therefore significant as a much needed applicable analysis tool to interpret broad experimental results and related applications.

Conflicts of interest

The authors declare no competing financial interests.

Acknowledgements

This material is based upon work supported by the U.S. Department of Energy, Office of Science, Office of Basic Energy Sciences under Award Number DE-SC0019043.

References

1 W.-L. Hsu and H. Daiguji, *Anal. Chem.*, 2016, **88**, 9251–9258.
2 P. Waduge, R. Hu, P. Bandarkar, H. Yamazaki, B. Cressiot, Q. Zhao, P. C. Whitford and M. Wanunu, *ACS Nano*, 2017, **11**, 5706–5716.
3 W. J. Lan, D. A. Holden, J. Liu and H. S. White, *J. Phys. Chem. C*, 2011, **115**, 18445–18452.
4 S. R. German, L. Luo, H. S. White and T. L. Mega, *J. Phys. Chem. C*, 2013, **117**, 703–711.
5 W. J. Lan, C. Kubeil, J. W. Xiong, A. Bund and H. S. White, *J. Phys. Chem. C*, 2014, **118**, 2726–2734.
6 Y. Qiu, I. Vlassiouk, Y. Chen and Z. S. Siwy, *Anal. Chem.*, 2016, **88**, 4917–4925.
7 E. Weatherall and G. R. Willmott, *J. Phys. Chem. B*, 2015, **119**, 5328–5335.
8 S.-M. Lu, Y.-Y. Peng, Y.-L. Ying and Y.-T. Long, *Anal. Chem.*, 2020, **92**, 5621–5644.
9 S.-M. Lu and Y.-T. Long, *TrAC, Trends Anal. Chem.*, 2019, **117**, 39–46.
10 R.-J. Yu, Y.-L. Ying, R. Gao and Y.-T. Long, *Angew. Chem., Int. Ed.*, 2019, **58**, 3706–3714.
11 A. R. Kneller, D. G. Haywood and S. C. Jacobson, *Anal. Chem.*, 2016, **88**, 6390–6394.
12 X. Wu, P. Ramiah Rajasekaran and C. R. Martin, *ACS Nano*, 2016, **10**, 4637–4643.
13 X. Wu, J. Experton, W. Xu and C. R. Martin, *Anal. Chem.*, 2018, **90**, 7715–7720.
14 M. Tagliazucchi and I. Szleifer, *Mater. Today*, 2015, **18**, 131–142.
15 E. Riccardi, J.-C. Wang and A. I. Liapis, *J. Chem. Phys.*, 2014, **140**, 084901.
16 Z. Zhang, X. Sui, P. Li, G. Xie, X.-Y. Kong, K. Xiao, L. Gao, L. Wen and L. Jiang, *J. Am. Chem. Soc.*, 2017, **139**, 8905–8914.
17 R. Long, Z. Kuang, Z. Liu and W. Liu, *Phys. Chem. Chem. Phys.*, 2018, **20**, 7295–7302.
18 R. B. Schoch, J. Han and P. Renaud, *Rev. Mod. Phys.*, 2008, **80**, 839–883.
19 Z. S. Siwy and S. Howorka, *Chem. Soc. Rev.*, 2010, **39**, 1115–1132.
20 E. Riccardi, J. C. Wang and A. I. Liapis, *J. Sep. Sci.*, 2012, **35**, 3073–3083.
21 C.-M. Wang, D.-L. Kong, Q. Chen and J.-M. Xue, *Frontiers of Materials Science*, 2013, **7**, 335–349.
22 J. Cai, Q. He, L. Song, L. Han, B. Liu, Y. Zhao, W. Chen and D. Zhan, *J. Phys. Chem. C*, 2019, **123**, 26299–26308.
23 D. C. Wang, M. Kvetny, J. Liu, W. Brown, Y. Li and G. L. Wang, *J. Am. Chem. Soc.*, 2012, **134**, 3651–3654.
24 D. C. Wang, W. Brown, Y. Li, M. Kvetny, J. Liu and G. L. Wang, *Anal. Chem.*, 2017, **89**, 11811–11817.
25 Y. Li, D. C. Wang, M. M. Kvetny, W. Brown, J. Liu and G. L. Wang, *Chem. Sci.*, 2015, **6**, 588–595.
26 D. Wang, J. Liu, M. Kvetny, Y. Li, W. Brown and G. Wang, *Chem. Sci.*, 2014, **5**, 1827–1832.
27 H. Daiguji, P. Yang and A. Majumdar, *Nano Lett.*, 2004, **4**, 137–142.
28 H. S. White and A. Bund, *Langmuir*, 2008, **24**, 2212–2218.
29 I. Vlassiouk, S. Smirnov and Z. Siwy, *ACS Nano*, 2008, **2**, 1589–1602.
30 Y. Ai, M. K. Zhang, S. W. Joo, M. A. Cheney and S. Z. Qian, *J. Phys. Chem. C*, 2010, **114**, 3883–3890.
31 J.-P. Hsu, S.-T. Yang, C.-Y. Lin and S. Tseng, *J. Phys. Chem. C*, 2017, **121**, 4576–4582.
32 S. Tseng, S.-C. Lin, C.-Y. Lin and J.-P. Hsu, *J. Phys. Chem. C*, 2016, **120**, 25620–25627.
33 D.-H. Lin, C.-Y. Lin, S. Tseng and J.-P. Hsu, *Nanoscale*, 2015, **7**, 14023–14031.
34 J.-P. Hsu, T.-W. Lin, C.-Y. Lin and S. Tseng, *J. Phys. Chem. C*, 2017, **121**, 28139–28147.

35 W. J. Lan, M. A. Edwards, L. Luo, R. T. Perera, X. J. Wu, C. R. Martin and H. S. White, *Acc. Chem. Res.*, 2016, **49**, 2605–2613.
36 E. C. Yusko, R. An and M. Mayer, *ACS Nano*, 2010, **4**, 477–487.
37 Y. Qiu, R. A. Lucas and Z. S. Siwy, *J. Phys. Chem. Lett.*, 2017, **8**, 3846–3852.
38 N. Laohakunakorn, B. Gollnick, F. Moreno-Herrero, D. G. A. L. Aarts, R. P. A. Dullens, S. Ghosal and U. F. Keyser, *Nano Lett.*, 2013, **13**, 5141–5146.
39 P. Jin, H. Mukaibo, L. P. Horne, G. W. Bishop and C. R. Martin, *J. Am. Chem. Soc.*, 2010, **132**, 2118–2119.
40 G. W. Bishop, M. M. Lopez, P. Ramiah Rajasekaran, X. Wu and C. R. Martin, *J. Phys. Chem. C*, 2015, **119**, 16633–16638.
41 L. Luo, D. A. Holden, W.-J. Lan and H. S. White, *ACS Nano*, 2012, **6**, 6507–6514.
42 L. Luo, D. A. Holden and H. S. White, *ACS Nano*, 2014, **8**, 3023–3030.
43 W.-J. Lan, D. A. Holden and H. S. White, *J. Am. Chem. Soc.*, 2011, **133**, 13300–13303.
44 D. Wang, W. Brown, Y. Li, M. Kvetny, J. Liu and G. Wang, *ChemElectroChem*, 2018, **5**, 3089–3095.
45 J. Liu, M. Kvetny, J. Feng, D. Wang, B. Wu, W. Brown and G. Wang, *Langmuir*, 2012, **28**, 1588–1595.
46 S. Pennathur and J. G. Santiago, *Anal. Chem.*, 2005, **77**, 6782–6789.
47 W. Guo, Y. Tian and L. Jiang, *Acc. Chem. Res.*, 2013, **46**, 2834–2846.
48 J. Liu, D. C. Wang, M. Kvetny, W. Brown, Y. Li and G. L. Wang, *Langmuir*, 2013, **29**, 8743–8752.
49 Y. Li, M. Kvetny, M. Bowen, W. Brown, D. Wang and G. Wang, *Cryst. Growth Des.*, 2019, **19**, 2470–2475.
50 L. Innes, M. R. Powell, I. Vlassiouk, C. Martens and Z. S. Siwy, *J. Phys. Chem. C*, 2010, **114**, 8126–8134.
51 E. V. Levine, M. M. Burns and J. A. Golovchenko, *Phys. Rev. E*, 2016, **93**, 013124.
52 F. Lopez Arbeloa, T. Lopez Arbeloa, M. J. Tapia Estevez and I. Lopez Arbeloa, *J. Chem. Phys.*, 1991, **95**, 2203–2208.